Theoretical HDO emission from low-mass protostellar envelopes

B. Parise, C. Ceccarelli, S. Maret

▶ **To cite this version:**

B. Parise, C. Ceccarelli, S. Maret. Theoretical HDO emission from low-mass protostellar envelopes. Astronomy and Astrophysics - A&A, 2005, 441, pp.171-179. 10.1051/0004-6361:20053081 . hal-00398171

HAL Id: hal-00398171
https://hal.science/hal-00398171

Submitted on 5 Jan 2023

HAL is a multi-disciplinary open access archive for the deposit and dissemination of scientific research documents, whether they are published or not. The documents may come from teaching and research institutions in France or abroad, or from public or private research centers.

L'archive ouverte pluridisciplinaire **HAL**, est destinée au dépôt et à la diffusion de documents scientifiques de niveau recherche, publiés ou non, émanant des établissements d'enseignement et de recherche français ou étrangers, des laboratoires publics ou privés.

A&A 441, 171–179 (2005)
DOI: 10.1051/0004-6361:20053081
© ESO 2005

Astronomy & Astrophysics

Theoretical HDO emission from low-mass protostellar envelopes⋆

B. Parise[1,⋆⋆], C. Ceccarelli[2], and S. Maret[3]

[1] CESR CNRS-UPS, BP 4346, 31028 Toulouse Cedex 04, France
e-mail: bparise@mpifr-bonn.mpg.de
[2] Laboratoire d'Astrophysique, Observatoire de Grenoble, BP 53, 38041 Grenoble Cedex 09, France
[3] Department of Astronomy, University of Michigan, 500 Church Street, Ann Arbor MI 48109-1042, USA

Received 17 March 2005 / Accepted 28 May 2005

Abstract. We present theoretical predictions of the rotational line emission of deuterated water in low-mass protostar collapsing envelopes. The model accounts for the density and temperature structure of the envelope, according to the inside-out collapse framework. The deuterated water abundance profile is approximated by a step function, with a low value in the cold outer envelope and a higher value in the inner envelope where the grain mantles evaporate. The two abundances are the two main parameters of the modeling, along with the temperature at which the mantles evaporate. We report line flux predictions for a 30 and 5 $L_\odot$ source luminosity respectively. We show that ground-based observations are capable of constraining the three parameters of the model in the case of bright low-mass protostars ($L > 10\ L_\odot$), and that no space-based observations, such as HSO observations, are required in this case. On the contrary, we show that the study of low-luminosity sources ($L < 10\ L_\odot$), assuming the same HDO abundance profile, requires too much integration time to be carried out either with available ground-based telescopes or with the HIFI instrument on board HSO. For these sources, only the large interferometer ALMA will allow one to constrain the HDO abundance.

Key words. ISM: abundances – ISM: molecules – stars: formation

1. Introduction

Water is a key molecule in the study of star formation for four main reasons. Since it has a large dipole, it has large spontaneous emission coefficients and high critical densities, which makes it a powerful diagnostic tool. Secondly, water is important in star forming regions for the role it plays in cooling the gas (Neufeld & Kaufman 1993), and, sometimes, also in heating it (e.g. Ceccarelli et al. 1996, hereinafter CTH96). Third, it is an important molecule from the chemical point of view, because in many circumstances it is the most abundant oxygen-bearing molecule, and, hence, it influences the abundance of all the more complex "trace" molecules; in other words, it influences the overall chemical composition of the gas (e.g. Rodgers & Charnley 2003). Finally, water is the most abundant component of grain mantles too (e.g. Gibb et al. 2004). For all these reasons, it is extremely important to know its abundance distribution in star forming regions. Unfortunately, the interstellar rotational water lines are absorbed by the water vapour of the Earth's atmosphere. Therefore, the observation of water vapour in astrophysical sources requires out-of-atmosphere instruments, like those on the satellites ISO, SWAS and ODIN, or the future satellite HSO, to be launched in 2007.

Fortunately, some rotational transitions of the deuterated form of water, HDO, are observable from ground-based telescopes, and can be used, under some circumstances, to probe the water content in astrophysical sources. Furthermore, HDO is an interesting molecule in itself, because it gives important information on the water formation and on the physical conditions of the observed region, either now or during the past. If formed on the grain surfaces during a previous phase, for example, and then released into the gas phase because of mantle evaporation due to the heating from a new-born star, the measured HDO abundance would reveal the past history of water formation. This is likely the case of what happens in solar type protostars. After a pre-collapse cold phase where the grain mantles are likely formed, either because of accretion of molecules onto the grain surfaces or because of the synthesis of the molecules on the grain surfaces, the molecules are released in the gas phase in the regions heated by the protostar radiation. Two classes of molecules show evidence of this process:

i) Hydrogenated molecules such as formaldehyde and methanol (Ceccarelli et al. 2000b; Schöier et al. 2002, 2004; Maret et al. 2004, 2005) and complex organic molecules, observed in the so-called "hot cores" (Cazaux et al. 2003; Bottinelli et al. 2004a,b; Kuan et al. 2004).

⋆ Appendices are only available in electronic form at http://www.edpsciences.org

⋆⋆ *Present address*: Max-Planck Institut für Radioastronomie, Auf dem Hügel 69, 53121 Bonn, Germany.

Article published by EDP Sciences and available at http://www.edpsciences.org/aa or http://dx.doi.org/10.1051/0004-6361:20053081

These molecules are not observed in the cold gas with large abundances measured in the inner regions of the envelopes surrounding solar-type protostars. Indeed, they are direct and indirect products of the grain mantle evaporation, so that they are linked to the pre-collapse phase.

ii) Deuterated molecules observed with extremely large abundances, which can only be formed during the cold, dense and CO depleted phase of the pre-collapse (Roberts & Millar 2000; Roberts et al. 2003). Notable examples are formaldehyde (Ceccarelli et al. 1998), methanol (Parise et al. 2002, 2004), hydrogenated sulfide (Vastel et al. 2003) and ammonia (Lis et al. 2002; van der Tak et al. 2002). HDO belongs to the second class of molecules, signs of the past pre-collapse phase. The above-mentioned molecules show extremely large deuteration ratios in low mass star-forming regions: singly deuterated molecules are more than 10% of their H-counterparts, whereas doubly and triply deuterated molecules can respectively be as high as 10% and ∼1%. On the contrary, HDO is only a relatively small fraction of H_2O, about 3% at best (Parise et al. 2005), and no D_2O has been detected so far, at relatively low upper limits to our knowledge (Cernicharo, private communication). The above relative small values agree with the non-detection of solid HDO in protostars (e.g. Dartois et al. 2003; Parise et al. 2003). Thus, there is evidence that water deuteration follows a different route with respect to the other molecules. In addition, the study of the available observations in IRAS 16293–2422 suggests that the deuteration ratio is not the same in the inner and outer envelope: 3% and ≤0.2% in the inner and outer envelope respectively (Parise et al. 2005). Thus, in order to better understand this difference, one needs to be able to disentangle where the different emissions come from. The present study aims at giving a theoretical tool for the estimate of the HDO abundance in protostellar envelopes, in the inner and outer regions, and, possibly, the evaporation temperature, and, consequently, at indicating the best observations to obtain this information. Specifically, given that the satellite HSO will be launched in 2007, particular care will be devoted to discussing whether observations with instruments on this satellite will be required to derive the HDO abundance and evaporation temperature in low mass protostellar envelopes, compared to observations that can be obtained with ground based telescopes.

The paper is organized as follows: we describe the adopted model and code in Sect. 2, we present the HDO molecule as well as the instruments available to observe its rotational spectrum in Sect. 3. We describe the general characteristics of the predicted spectrum in Sect. 4 and give the results in Sect. 5 for a relatively high (30 $L_\odot$) and low (5 $L_\odot$) luminosity case. Section 6 contains a discussion about the best lines to observe to derive the HDO abundance in the inner and outer envelope, as well as the HDO ice evaporation temperature. We also discuss the interest of carrying out space-based versus ground-based HDO observations to constrain these parameters.

2. The model description

The model used to compute the HDO emission in collapsing envelopes has been adapted from the original model developed by CHT96 to predict the OI, CO and H_2O line emission, and successively modified to compute the H_2CO line emission (Ceccarelli et al. 2003). Here we describe the basic assumptions of the model.

The envelope density structure and dynamics are assumed to follow the "inside-out" collapse picture (Shu 1977), for a spherical initial isothermal sphere undergoing collapse. In the outer envelope, not yet affected by the collapse, the molecular hydrogen number density distribution $n_{\rm H_2}(r)$ is given by:

$$n_{\rm H_2}(r) = \frac{a^2}{2\pi\mu m_{\rm H} G} r^{-2} = 2.8\times10^8 \left(\frac{a}{0.35\ {\rm km\ s^{-1}}}\right)^2 r_{100\ {\rm AU}}^{-2}\ {\rm cm^{-3}} \quad (1)$$

where a is the sound speed, $m_{\rm H}$ is the hydrogen mass, μ is the mean molecular mass in amu units, equal to 2.8, $r_{100\ {\rm AU}}$ is the distance from the center in 100 AU units, and G is the gravitational constant. In the inner collapsing regions the density is described by the free-fall solution:

$$n_{\rm H_2}(r) = \frac{1}{4\pi\mu m_{\rm H}} \left(\frac{\dot{M}^2}{2GM_\star}\right)^{\frac{1}{2}} r^{-\frac{3}{2}} \quad (2)$$

$$= 1.2\times10^7 \left(\frac{\dot{M}^2_{-5}}{M_\star r^3_{100\ {\rm AU}}}\right)^{\frac{1}{2}}\ {\rm cm^{-3}}. \quad (3)$$

The free fall velocity is given:

$$v(r) = \left(\frac{2GM_\star}{r}\right)^{\frac{1}{2}} = 4.2\left(\frac{M_{\star 1}}{r_{100\ {\rm AU}}}\right)^{\frac{1}{2}}\ {\rm km\ s^{-1}}, \quad (4)$$

where $\dot{M}$ is the mass accretion rate, related to the sound speed by

$$\dot{M} = 0.975\frac{a^3}{G} = 10^{-5}\left(\frac{a}{0.35\ {\rm km\ s^{-1}}}\right)^3\ M_\odot\ {\rm yr^{-1}}. \quad (5)$$

$\dot{M}_{-5}$ is $\dot{M}$ in units of $10^{-5}\ M_\odot\ {\rm yr^{-1}}$, and $M_{\star 1}$ is the mass of the central object $M_\star$ in units of 1 $M_\odot$. The gravitational energy of the collapsed mass is released radiatively as material falls onto the core radius $R_\star$, so that the luminosity of the central object is:

$$L_\star = \frac{GM_\star\dot{M}}{R_\star} = 22\left(\frac{M_\star}{M_\odot}\right)\dot{M}_{-5}\ R_{12}^{-1}\ L_\odot \quad (6)$$

where $R_{12} = R_\star/10^{12}$ cm.

The spherical symmetry is conserved throughout the collapse in this model. In this sense, the model gives accurate results only for that part of the envelope in which spherical symmetry is a good approximation, i.e. probably for radii larger than a few tens of AUs (Ceccarelli et al. 2000a). At smaller scales large deviations from the spherical symmetry are expected because of the presence of a circumstellar disk.

The gas temperature is computed self-consistently by equating the cooling and heating mechanisms at each point

of the envelope. Details of these calculations can be found in CHT96. The cooling depends on the abundance of the atomic oxygen, CO and H_2O, namely the main gas coolants across the envelope. Hence their abundances are hidden parameters of the model. The resulting gas temperature tracks the dust temperature very closely across the envelope, except where the icy mantles evaporate. Because of the injection of large quantities of water in the gas phase and the consequent enhancement of the gas cooling, the gas and dust (thermally) decouple in a relatively small region after the icy mantles evaporation (see also for example Maret et al. 2002).

Ceccarelli et al. (2000a) and Maret et al. (2002) demonstrated that the gas temperature differs by no more than 10% from the dust temperature, and this occurs in a relatively small region just next to where the ices sublimate. There is some uncertainty about the water and oxygen abundances in protostars, as derivations of the H_2O abundance has been obtained in two sources only, IRAS 16293 and NGC 1333–IRAS4 (Ceccarelli et al. 2000a; Maret et al. 2002). However, these uncertainties do not much affect the gas temperature derivation, as in the outer envelope the gas is cooled mostly by CO[1], and in the inner envelope it is cooled by the sublimated water. At the same time, in the inner region the heating of the gas is dominated by the collisional de-excitation of the water molecules, photopumped by the photons emitted by the innermost warm dust (CHT96), so that the coupling between the dust and gas is always ensured. As a result, the HDO computed line intensity is insensitive to these uncertainties.

The original CHT96 model is time-dependent, but the authors demonstrated that the physical structure and water chemistry can be computed at each time independently of the previous history, once the luminosity and the mass of the protostar are known. The reason for this is that in the outer cold envelope the abundance of the water is practically constant with time, whereas in the inner warm envelope the water abundance is set by the ice evaporation, except in the very inner regions where the temperature exceeds 250 K. Since the sizes of the evaporation region are set by the temperature and the density profile, for practical applications to real sources one needs to input them only. The velocity field is also needed to compute the line intensity, and this can be derived as well from observations.

For the standard case described in Sect. 4, we considered the case of IRAS 16293, whose velocity, density and temperature profiles have been derived by several authors from actual observations. The computations shown in Figs. 2–7 adopted the profile derived in Ceccarelli et al. (2000a). We also studied the case of a low luminosity source, and we used the velocity, density and temperature profiles derived for the source L1448 mm by Maret et al. (2004).

We approximate the HDO abundance profile with a step function. In the outer envelope the HDO abundance, $x_{\rm cold}$, is relatively low and similar to that observed in molecular clouds. In the innermost regions of the envelope, where the dust reaches the evaporation temperature $T_{\rm evap}$, the HDO abundance, $x_{\rm warm}$, jumps to larger values. These last three parameters – $x_{\rm cold}$, $x_{\rm warm}$ and $T_{\rm evap}$ – are the three free parameters of the present modeling, and they will be varied to study their influence on the HDO line emission.

[1] The CO lines are optically thick and, therefore, the cooling function does not depend on the CO abundance unless it decreases by a factor of 100 with respect to the standard value.

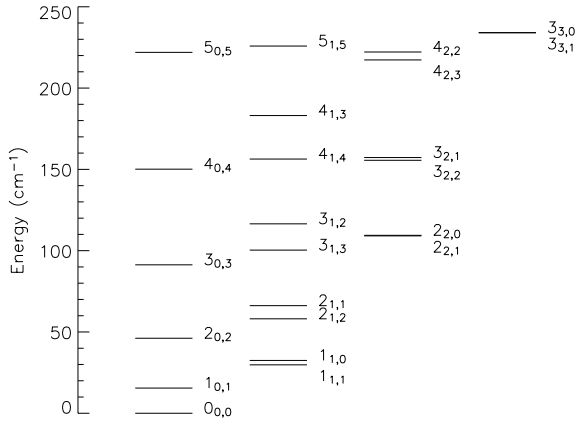

Fig. 1. First energy levels for the HDO molecule.

Low-mass protostars exhibit energetic molecular outflows, where the gas can be very hot (up to 2000 K, as testified by the H_2 rovibrational emission observed in several outflows). This gas could in principle contribute to the HDO line emission, so that it is important to evaluate whether the outflow emission can be comparable to or even larger than the HDO emission from the envelope. From a theoretical point of view, since molecular deuteration decreases exponentially with increasing gas temperature, the HDO abundance is expected to be very low in the warm gas of molecular outflows (see also Bergin et al. 1999). To support these theoretical expectations, observations of outflows on several low-mass protostars have revealed no HDO emission, at a level at least 10 times fainter than towards the protostar (IRAS 16293, Parise et al. 2005; NGC 1333–IRAS2 and IRAS4A, Caux et al. in prep.). We therefore decided to consider in the present study only the envelope contribution to the HDO emission.

All the line fluxes are computed for a source at a distance of 160 pc. The model computes the level population of the first 34 levels of the HDO. The molecular data are from the JPL catalogue (`http://spec.jpl.nasa.gov/home.html`), and the collisional coefficients are from Green (1989), for He-HDO collisions between 50 and 500 K, scaled for collision with H_2. Note that all abundances are reported here with respect to H_2.

3. The HDO rotational line spectrum

3.1. The energy levels

HDO is a planar assymetric top molecule. Its dipole lies along its a and b axies, with dipole moments $\mu_a = 0.657$ and $\mu_b = 1.732$ Debye (Clough et al. 1973). The allowed transitions are thus a-type and b-type transitions:

$$\Delta K_a = 0 \ \text{ and } \ \Delta K_c = \pm 1$$

or

$$\Delta K_a = \pm 1 \ \text{ and } \ \Delta K_c = \pm 1.$$

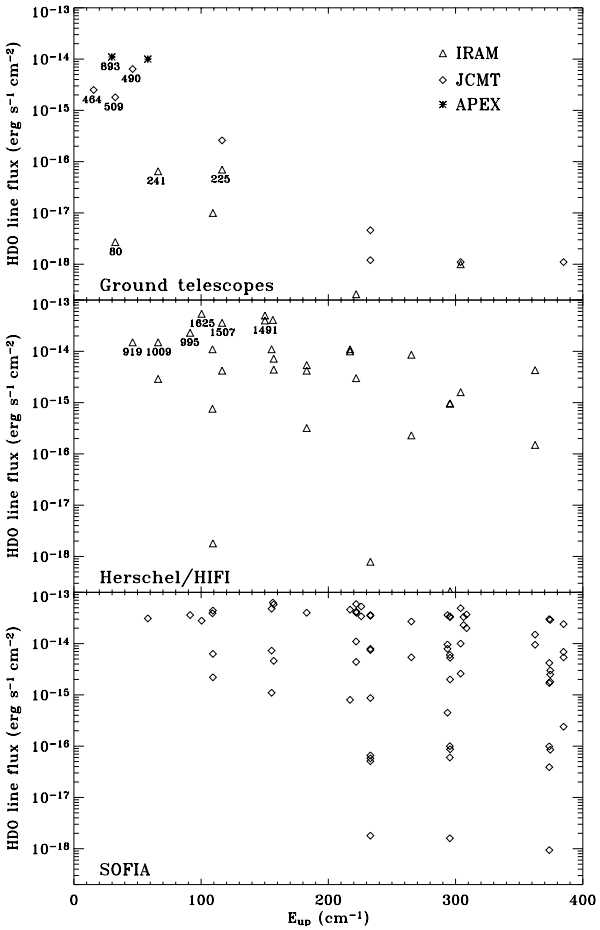

Fig. 2. HDO line fluxes predicted for the test case IRAS 16293−2422 versus the upper level energy of the transition. The upper panel presents the transitions observable from the ground, the middle panel the transitions observable with HSO/HIFI and the lower panel the transitions observable with SOFIA. The frequencies of the transitions that are going to be studied in more detail are indicated in GHz.

The first energy levels for HDO are presented in Fig. 1.

The list of the transitions between the first 34 levels is reported in Table A.1.

3.2. The observing instruments

We detail in this section the instruments that operate (or will operate in the near-future) in the frequency bands interesting for the HDO observations.

a) Ground telescopes

Several ground based facilities allow to observe the HDO rotational spectrum transitions.
The IRAM (Institute for Millimetre Radioastronomy) 30 m telescope (Pico Veleta, Spain) operates between 80 and 281 GHz.

The 15 m JCMT dish (James Clerk Maxwell Telescope, Mauna Kea, Hawaii) observes in the 230, 345, 450, and 650 GHz frequency bands. The 800 GHz instrument is no longer available, but this frequency range will be observable with APEX.

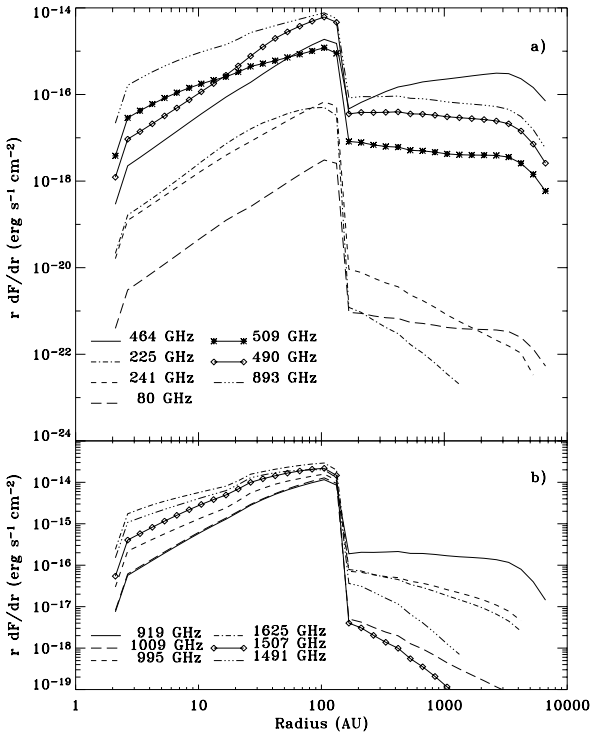

Fig. 3. Contribution to the line intensity as function of the distance from the central source, for seven HDO lines observable from the ground (*upper panel*) and six from space based telescopes (*lower panel*).

The 10 m CSO dish (Caltech Submillimeter Observatory, Mauna Kea, Hawaii) operates roughly in the same frequency bands as JCMT.

The 15 m APEX dish (Atacama Pathfinder EXperiment, Chajnantor, Chile) is being built on the ALMA site. It will allow observations in the 230, 345, 650 and 850 GHz bands.

b) Airborne instruments: SOFIA

The 2.5 m telescope of the Stratospheric Observatory for Infrared Astronomy, on board a Boeing 747, will be equipped with several interesting instruments for HDO observation. In particular, CASIMIR (CAltech Submillimeter Interstellar Medium Investigations Receiver), will observe in the 500–2100 GHz band and GREAT (German REceiver for Astronomy at Terahertz frequencies) in the 1.5–5 THz.

c) The HSO satellite

The HIFI (Heterodyne Instrument for the Far-Infrared) instrument on board Herschel Space Observatory (launch planned in 2007) will allow observations in the 480–1250 and 1410–1910 GHz bands.

4. Model results

We first report the computed HDO line spectrum of a test case, to illustrate the general characteristics of the predicted spectrum. Then, in the following paragraphs we discuss thoroughly how the HDO line spectrum varies with the three free parameters of the model, namely the HDO abundance in the outer

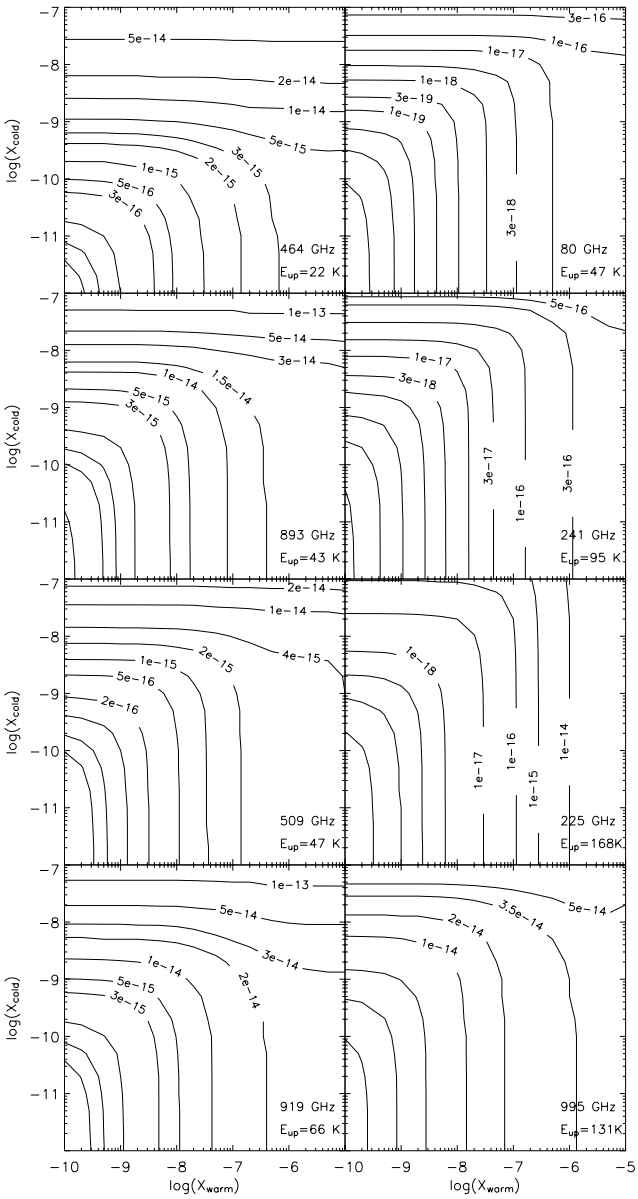

Fig. 4. Line intensity as a function of the HDO abundance in the outer and inner regions of the envelope, $x_{\rm cold}$ and $x_{\rm warm}$ respectively, for the eight HDO transitions at 464, 893, 509, 80, 241, 225, 919 and 995 GHz respectively. The first six lines are observable from the ground, whereas the last two ones will be observable with the Herschel telescope. Line fluxes are in erg s^{-1} cm^{-2}. In these calculations the mantle evaporation temperature is 100 K.

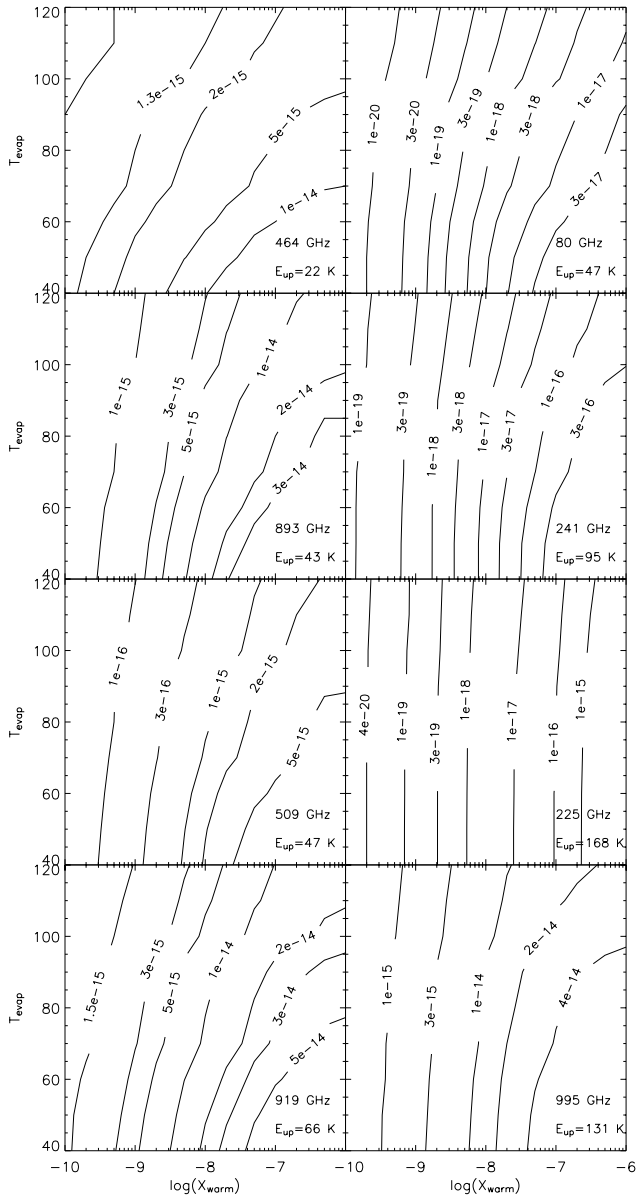

Fig. 5. Predicted flux for the eight transitions depending on the assumed evaporation temperature and inner HDO abundance for an outer abundance $x_{\rm cold}$ fixed to 2×10^{-10}.

cold envelope $x_{\rm cold}$, in the inner warm envelope $x_{\rm warm}$ and the evaporation temperature $T_{\rm evap}$.

The parameters adopted in the test case are reported in Table 1. The values of the hidden parameters are the same as the test case shown in Ceccarelli et al. (2003) for discussing the H_2CO line emission, and have been derived from several observations of IRAS 16293–2422. The $x_{\rm cold}$, $x_{\rm warm}$ and $T_{\rm evap}$ parameters have also been derived by the analysis of the HDO observations towards IRAS 16293–2422 (Parise et al. 2005). In the following all fluxes are given in erg s^{-1} cm^{-2} and are the integrated emission over the entire envelope for a source at 160 parsecs. Although the conversion in K km s^{-1} would have been more convenient for the observers, the signal in K km s^{-1} depends on the beam of the telescope used for the observation and how it matches the predicted extent of the emission. We will give the K km s^{-1} signal for a few lines, when considering the application to observations with ground versus space based instruments (Sect. 5).

Table A.1 reports the predicted fluxes of the HDO lines for the test case, and Fig. 2 shows the line fluxes as a function of the upper energy of the transition.

The transitions have been labeled according to the available observing facility. The lowest lying levels are observable from the ground and space borne observations become competitive for upper energies greater than 50 cm^{-1}.

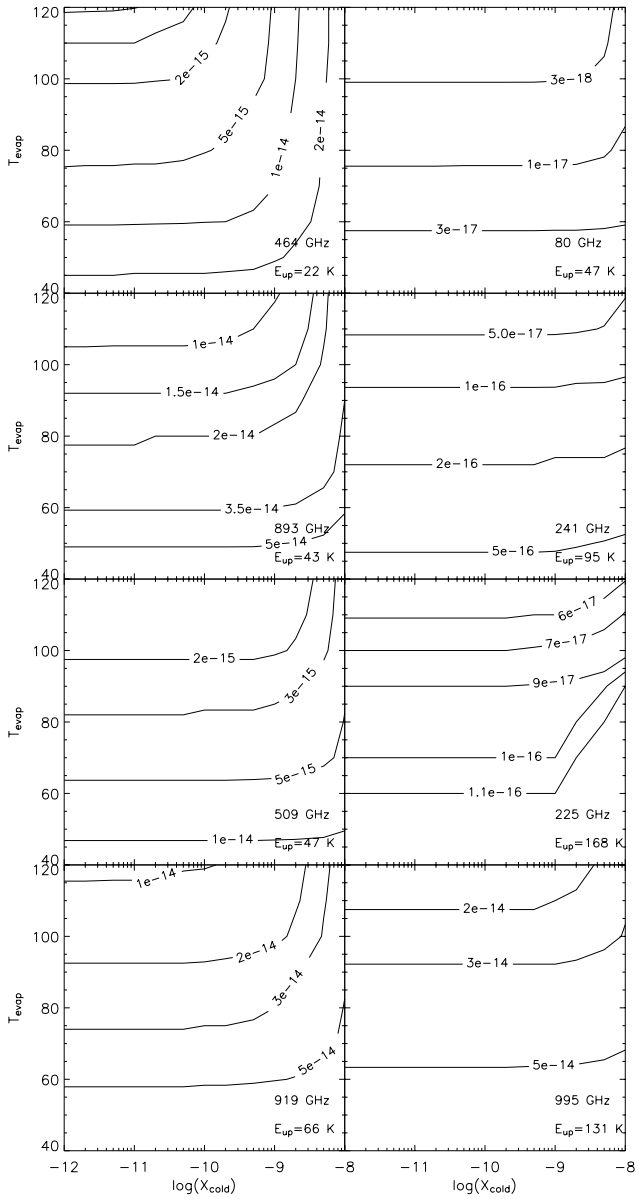

Fig. 6. Predicted flux for the eight transitions depending on the assumed evaporation temperature and outer HDO abundance for an inner abundance $x_{\rm warm}$ fixed to 10^{-7}.

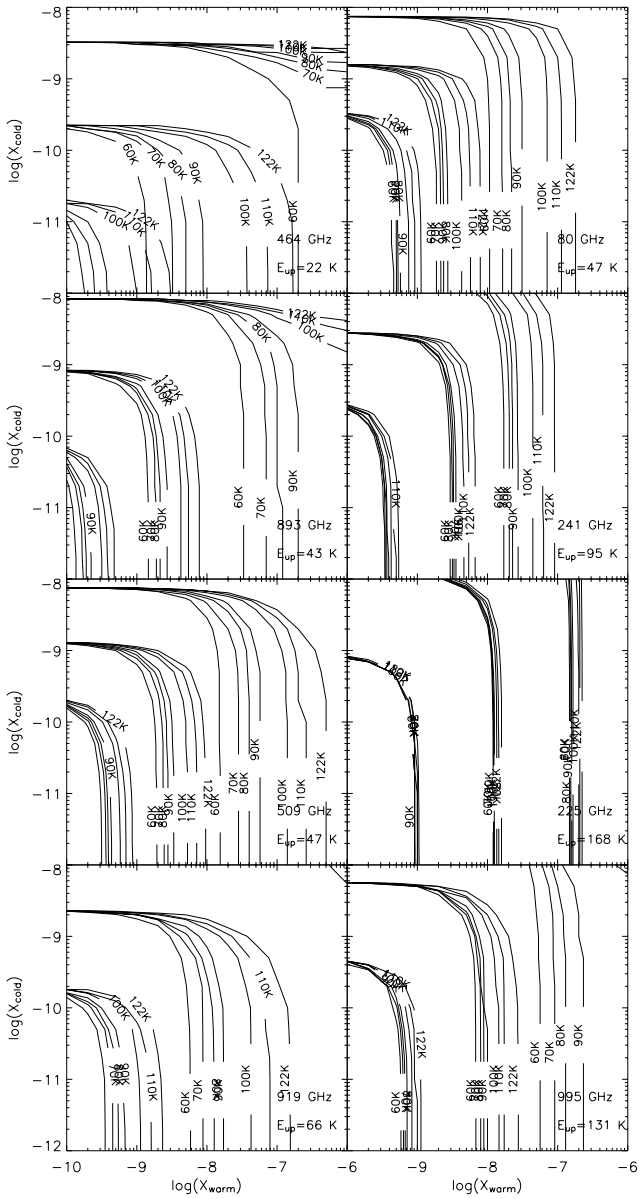

Fig. 7. Evaporation temperature dependence in a $x_{\rm warm}$–$x_{\rm cold}$ diagram. For each transition, the three groups of curves correspond to the contour for three different values of the line flux. The different curves for each group correspond to different values of the evaporation temperature. A narrow group of curves implies that the uncertainty on the evaporation temperature value will not affect much the estimation of $x_{\rm warm}$ and $x_{\rm cold}$.

Figure 3 shows the contribution to the emission from different shells of the envelope for several transitions with different upper energy levels, observable with ground-based telescopes (upper panel) or with Herschel-HIFI (lower panel). Note that the 893 GHz line has been included in the upper panel as it will be observable with the APEX facility. Some of the lines have been observed towards IRAS 16293−2422 using the JCMT and the IRAM 30 m telescopes (80, 225, 241 and 464 GHz, Parise et al. 2005). The other ones have been chosen because they are potentially bright lines (Fig. 2), spanning upper energy levels up to 150 cm^{-1} (∼200 K). This figure illustrates that the relative contribution to the line intensity from the inner region ($r \leq 150$ AU) increases with increasing upper level energy of the transition. While all line intensities are dominated by the emission in the inner region (where the abundance is about 3 orders of magnitude higher), the lines with low upper level energy exhibit a relatively high contribution from the cold outer envelope.

4.1. Varying the parameters

In this paragraph, we show how the HDO line spectrum changes varying the three free parameters of the model, namely the HDO abundance in the outer and inner parts of the envelope, $x_{\rm cold}$ and $x_{\rm warm}$ respectively, and the mantle evaporation temperature $T_{\rm evap}$.

Table 1. Values of the parameters adopted for the test case. The upper part reports the values of the three free parameters of the model, whereas the lower part reports the value of the hidden parameters.

Parameter	Value
$x_{\rm warm}$	1×10^{-7}
$x_{\rm cold}$	1.5×10^{-10}
$T_{\rm evap}$	100 K
$M_\star$	0.8 $M_\odot$
$\dot{M}$	3×10^{-5} $M_\odot$ yr^{-1}
x(CO)	1×10^{-4}
x(O)	2.5×10^{-4}
$x_{\rm cold}(H_2O)$	5×10^{-7}
$x_{\rm warm}(H_2O)$	3×10^{-6}

a) $x_{\rm cold}$ *and* $x_{\rm warm}$

Figure 4 shows the line intensities of eight HDO lines (including two lines observable with Herschel-HIFI) for $x_{\rm cold}$ varying from 10^{-7} to 10^{-12} and $x_{\rm warm}$ varying from 10^{-5} to 10^{-10}. As expected, the intensities of the lower level transitions are mostly sensitive to the emission from the cold part of the envelope, as long as the outer abundance of HDO is not too low compared to the inner abundance. For instance the 464 GHz line is sensitive to $x_{\rm cold}$ even for inner abundances up to two orders of magnitude larger. On the contrary, the higher the upper energy, the more the transition becomes dependent on the inner parts of the envelope.

The figures also show that the low lying lines are much less sensitive in general to the variation of $x_{\rm warm}$ (a factor 50 at most varying $x_{\rm warm}$ by four orders of magnitude) with respect to the high lying lines. The latter vary almost linearly with $x_{\rm warm}$, so they are clearly better suited to constrain this parameter than the low lying lines. On the other hand, $x_{\rm cold}$ is better constrained by the low lying lines, and particularly by the 464 GHz one, which shows the largest variation, nearly 2 orders of magnitude for a change of $x_{\rm cold}$ of two orders of magnitude.

b) $T_{\rm evap}$

Figures 5 and 6 present the predicted fluxes depending on the evaporation temperature and respectively the inner and the outer abundances. The higher the evaporation temperature, the higher the inner abundance must be to reproduce the same flux. Indeed, the higher the evaporation temperature, the less extended the inner region.

The 225 GHz line is mostly independant of the evaporation temperature in the studied range (Fig 5). Indeed this line has the highest upper energy (∼170 K) and is likely to be mostly excited in the innermost region of the envelope. Thus it does not depend on the evaporation temperature, as long as this temperature is much lower than 170 K, nor on $x_{\rm cold}$. This line is thus only sensitive to the inner abundance.

Another way to understand the dependance of the emission versus the evaporation temperature is to plot the regions spanned when varying the evaporation temperature for a fixed emission flux in a $x_{\rm cold}$–$x_{\rm warm}$ diagram (Fig. 7).

As expected, for low inner HDO abundances, the effect of the evaporation temperature is negligible, but curves begin to separate for high $x_{\rm warm}$. The uncertainty in the evaporation temperature mostly translates into an uncertainty in $x_{\rm warm}$. A remarquable point here is again that the 225 GHz emission is independent of the temperature.

Figure 5 shows that the line fluxes depend much more on $x_{\rm warm}$ than on $T_{\rm evap}$. Actually, based in Figs. 5 and 6, it seems very difficult to find a way to constrain $T_{\rm evap}$. However, Fig. 7 gives a sense of how the two parameters likely can be constrained. The 225 GHz line flux in practice can be used to estimate $x_{\rm warm}$ (Figs. 6 and 7), irrespective of $T_{\rm evap}$, whereas one can use, for example, the 464, the 80 and/or the 509 GHz line fluxes to estimate $T_{\rm evap}$, knowing $x_{\rm warm}$, from Fig. 7. Evidently, it is not possible to easily disentangle the three parameters, but the above analysis suggests that a full modeling can possibly succeed.

5. Applications

5.1. IRAS 16293–2422

In this section we give some practical recipes to derive, to a first approximation, the values of the parameters of the model from actual observations. However, the described method will just give some approximate estimates of the parameter values, and a full modeling of the source is necessary to derive more precise estimates.

As a practical example, we will use the data obtained towards IRAS 16293–2422 (Stark et al. 2004; Parise et al. 2005) and we will derive the approximate values of $x_{\rm cold}$ and $x_{\rm warm}$. We will then compare these results with those obtained with full modeling of the HDO emission from this source, as described in Parise et al. (2005).

First, to facilitate the comparison, Table 2 reports the conversion factor of the line intensity in erg s^{-1} cm^{-2} into the velocity-integrated main beam temperature $T_{\rm mb}\Delta v$ observed at the IRAM and JCMT telescopes respectively, for the five lines observed towards IRAS 16293−2422 (Parise et al. 2005). *Note that this is simply a conversion table, which does not take into account the convolution of the predicted emission with the telescope beam.* This is strictly valid for a point-like source with respect to the telescope beam sizes. The convolution with the beam can introduce large factors of difference if the emission originates in a region larger than that encompassed by the beam used, as may be the case for low-lying lines. In those cases, in order to use the plots of this article, the observer should take care to integrate the emission over the entire emitting region.

Parise et al. (2005) performed a full analysis of the HDO emission towards IRAS 16293−2422. We describe however how the tools we have given here allow us to approximately derive the envelope parameters. According to Fig. 7, the emission of the 225 GHz line, as well as the upper limit on the $x_{\rm cold}$ derived from the 464 GHz line, do not depend on the evaporation temperature. We can then use Fig. 4 (computed for an evaporation temperature of 100 K) to derive an upper limit on $x_{\rm cold}$ from the 464 GHz line. Parise et al. (2005) measured a line intensity of 5.5 K km s^{-1}. Using the conversion factor given in Table 2, this corresponds to 2.2×10^{-15} erg s^{-1} cm^{-2}. We deduce from Fig. 4 that $x_{\rm cold}$ is lower than a few 10^{-10}

Table 2. Conversion factors of the line intensity in erg s^{-1} cm^{-2} into the velocity integrated main beam temperature $T_{\rm mb}\Delta v$ observed at the IRAM and JCMT telescopes respectively, for the five lines observed towards IRAS 16293−2422 (Parise et al. 2005). Last column quotes the $T_{\rm mb}\Delta v$ observed towards IRAS 16293–2422 (Parise et al. 2005).[a] Predicted flux from the model simply converted into K km s^{-1} using the conversion factor. [b] Predicted flux derived using an accurate convolution of the signal with the telescope beam.

Transition	Frequency (GHz)	Telescope	Conversion coeff 1 K km s^{-1} ($T_{\rm mb}\Delta v$) (erg s^{-1} cm^{-2})	IRAS 16293–2422 (K km s^{-1}) Conversion[a]	(K km s^{-1}) Convolution[b]	(K km s^{-1}) Obs[c]
$1_{1,0}-1_{1,1}$	80.578	IRAM	1.4×10^{-17}	0.19	0.21	0.40
$3_{1,2}-2_{2,1}$	225.897	IRAM	4.1×10^{-17}	1.7	1.8	1.7
$2_{1,1}-2_{1,2}$	241.561	IRAM	4.4×10^{-17}	1.5	1.5	2.0
$2_{2,0}-3_{1,3}$	266.161	IRAM	4.9×10^{-17}	0.20	0.22	0.21
$1_{0,1}-0_{0,0}$	464.924	JCMT	4.0×10^{-16}	6.3	5.4	5.5

to 10^{-9}. The 225 GHz line emission then allows us to constrain the value of $x_{\rm warm}$ (independantly of the evaporation temperature). Indeed, converting the intensity observed by Parise et al. (2005), we find 7×10^{-17} erg s^{-1} cm^{-2}, which with the condition $x_{\rm cold}$ lower than 10^{-9}, constrains the abundance of HDO in the warm envelope to a value around 10^{-7}. The full modeling leads to $x_{\rm warm} = (1\pm0.3)\times10^{-7}$, and to a 3σ upper limit on $x_{\rm cold}$ of 10^{-9} (Parise et al. 2005).

Table 2 compares the predicted fluxes derived from the model by both using the simple conversion flux for a point-like source and an accurate convolution with the telescope (IRAM or JCMT) beam, to the observations performed towards IRAS 16293−2422 (Parise et al. 2005). As expected the simple conversion works reasonably well for the high-lying lines, as they originate from the small inner envelope (small enough compared to the beam size to be approximated by a point). The accuracy of the conversion for the ground line at 464 GHz is less good as some of the emission originates from the outer envelope, which is affected by the convolution of the telescope beam. Nevertheless the simple conversion is still accurate to 15% because for this testcase, the HDO abundance is three orders of magnitude lower in the outer envelope than the inner envelope. The conversion would become critical when the abundance in the cold envelope is not low compared to the warm contribution.

The plots of Figs. 4–6 can be used with single dish observations without the need for convolution, for the signal, originating in the warm part of the envelope, is likely to be encompassed by the telescope beam.

5.2. The low luminosity source case: L1448 mm

The previous predictions are of course dependent on the physical structure considered for the source. As an example, we also plotted the contours for a low-luminosity source, L1448 mm, for which physical characteristics can be found in Jørgensen et al. (2002) or Maret et al. (2004). The results are presented in Appendix B. The contours roughly look the same, except that the emission is weaker in L1448 mm.

5.3. Are space-based telescope observations towards low-mass protostars necessary?

We saw in the previous sections that the observation of the studied lines from the ground allows one to perfectly constrain the inner HDO abundance. However, the outer HDO abundance can only be constrained using lower energy transitions. Among the studied lines, only the 464 GHz can provide, in some specific conditions (namely when the outer abundance is not too low compared with the inner abundance) some information on $x_{\rm cold}$. Unfortunately, the transitions that will be observable from space are at higher energy (see Fig. 2). They will hence only provide information on the inner abundance, which is already correctly constrained with the transitions observed with ground-based telescopes. Moreover observations from the ground, when possible, have to be preferred owing to the better spatial resolution. Table 3 lists the integration time required to observe some selected transitions with a peak signal to noise of 5, at a resolution of 0.5 km s^{-1}, with the various instruments IRAM 30 m, JCMT and HSO/HIFI. Note that in each case, only one receiver was assumed (single polarization mode) so that the integration time could in principle be lowered by a factor of $\sqrt{2}$ if the observations are carried out in double polarization mode. An average of 2 mm of water vapor has been assumed at the IRAM 30 m, where the average elevation of the source is 25° and 70° respectively for IRAS 16293 and L1448 mm. Weather band 2 was assumed at JCMT, with a zenith angle of 40 and 20 respectively. An efficiency factor of 0.125 was assumed for HIFI, as predicted in chopping mode.

These predictions show that for sources as bright as IRAS 16293, observations can be carried out from the ground, and no Herschel time is thus necessary. But in the case of a low-luminosity protostar, where the same abundance profile of HDO was assumed, integration times start to become prohibitive from the ground. The 225 and 241 GHz lines may remain observable, using double polarisation receivers. Note that the integration time required with HIFI is prohibitive, the only reasonable transition being the 995 GHz. Thus, in the case of low-luminosity source, neither ground-based telescopes nor HSO/HIFI seem to be sensitive enough. The interferometer ALMA might provide in this case the only possibility of constraining the HDO abundance.

Table 3. Integration time required to detect the HDO lines with a peak signal over noise of 5 (see text). Note that only one receiver was assumed, so in principle those times can be lowered by a factor $\sqrt{2}$ by using a double polarization setup.

Transition	IRAM 30 m	JCMT	HSO/HIFI
IRAS 16293 (30 $L_\odot$)			
80 GHz	5.6 h		
225 GHz	15 min		
241 GHz	30 min		
464 GHz		29 min	
490 GHz		21 min	7 min
509 GHz		34 h*	104 min
893 GHz			16 min
995 GHz			5 min
L1448 mm (5 $L_\odot$)			
80 GHz	3500 h		
225 GHz	110 h		
241 GHz	227 h		
464 GHz		185 h	
490 GHz		132 h	73 h
509 GHz		1562 h *	471 h
893 GHz			59 h
995 GHz			16 h

* The sensibility drops on the edge of the band.

6. Conclusions

We reported theoretical predictions of the deuterated water line emission from the envelopes of low mass protostars. In this study, we have focused only on the envelope emission, neglecting any HDO emission from the outflows, which is expected to be of minor importance based on theoretical and observational arguments. We have shown that the simultaneous observations of appropriately selected transitions permit us to approximately constrain the HDO abundance in the outer cold and inner warm parts of the envelope. The uncertainty on the evaporation temperature mostly translates into an uncertainty on the inner abundance. The inner abundance can however be quite accurately determined using the 225 GHz line for which the emission has been shown to be independent of the evaporation temperature.

The most important result of the present study is that, for bright low-mass protostars ($L > 10\,L_\odot$), observations feasible from ground telescopes are sufficient to constrain the HDO abundance profile and evaporation temperature, and no HSO observations are required. In the case of low-luminosity protostars ($L < 10\,L_\odot$), both present ground-based telescopes and HSO seem to lack the sensitivity necessary to observe HDO lines in a reasonable integration time. The HDO abundance profile and evaporation temperature will probably be directly constrained by future high resolution observations with the large sub/millimeter interferometer ALMA.

Acknowledgements. We wish to thank the anonymous referee for very useful comments that helped to improve this article.

References

Bergin, E. A., Neufeld, D. A., & Melnick, G. J. 1999, ApJ, 510, L145
Bottinelli, S., Ceccarelli, C., Lefloch, B., et al. 2004a, ApJ, 615, 354
Bottinelli, S., Ceccarelli, C., Neri, R., et al. 2004b, ApJ, 617, L69
Caux, E., et al. in prep., A&A
Cazaux, S., Tielens, A. G. G. M., Ceccarelli, C., et al. 2003, ApJ, 593, L51
Ceccarelli, C., Hollenbach, D. J., & Tielens, A. G. G. M. 1996, ApJ, 471, 400
Ceccarelli, C., Castets, A., Loinard, L., Caux, E., & Tielens, A. G. G. M. 1998, A&A, 338, L43
Ceccarelli, C., Castets, A., Caux, E., et al. 2000a, A&A, 355, 1129
Ceccarelli, C., Loinard, L., Castets, A., Tielens, A. G. G. M., & Caux, E. 2000b, A&A, 357, L9
Ceccarelli, C., Maret, S., Tielens, A. G. G. M., Castets, A., & Caux, E. 2003, A&A, 410, 587
Clough, S. A., Beers, Y., Klein, G. P., & Rothman, L. S. 1973, J. Chem. Phys., 59, 2254
Dartois, E., Thi, W.-F., Geballe, T. R., et al. 2003, A&A, 399, 1009
Gibb, E. L., Whittet, D. C. B., Boogert, A. C. A., & Tielens, A. G. G. M. 2004, ApJS, 151, 35
Green, S. 1989, ApJS, 70, 813
Jørgensen, J. K., Schöier, F. L., & van Dishoeck, E. F. 2002, A&A, 389, 908
Kuan, Y., Huang, H., Charnley, S. B., et al. 2004, ApJ, 616, L27
Lis, D. C., Roueff, E., Gérin, M., et al. 2002, ApJ, 571, L55
Maret, S., Ceccarelli, C., Caux, E., Tielens, A. G. G. M., & Castets, A. 2002, A&A, 395, 573
Maret, S., Ceccarelli, C., Caux, E., et al. 2004, A&A, 416, 577
Maret, S., Ceccarelli, C., Tielens, A., et al. 2005, A&A, submitted
Neufeld, D. A., & Kaufman, M. J. 1993, ApJ, 418, 263
Parise, B., Ceccarelli, C., Tielens, A. G. G. M., et al. 2002, A&A, 393, L49
Parise, B., Simon, T., Caux, E., et al. 2003, A&A, 410, 897
Parise, B., Castets, A., Herbst, E., et al. 2004, A&A, 416, 159
Parise, B., Caux, E., Castets, A., et al. 2005, A&A, 431, 547
Roberts, H., & Millar, T. J. 2000, A&A, 361, 388
Roberts, H., Herbst, E., & Millar, T. J. 2003, ApJ, 591, L41
Rodgers, S. D., & Charnley, S. B. 2003, ApJ, 585, 355
Schöier, F. L., Jørgensen, J. K., van Dishoeck, E. F., & Blake, G. A. 2002, A&A, 390, 1001
Schöier, F. L., Jørgensen, J. K., van Dishoeck, E. F., & Blake, G. A. 2004, A&A, 418, 185
Shu, F. H. 1977, ApJ, 214, 488
Stark, R., Sandell, G., Beck, S. C., et al. 2004, ApJ, 608, 341
van der Tak, F. F. S., Schilke, P., Müller, H. S. P., et al. 2002, A&A, 388, L53
Vastel, C., Phillips, T. G., Ceccarelli, C., & Pearson, J. 2003, ApJ, 593, L97

Online Material

Appendix A: The predicted fluxes for the test case of IRAS 16293−2422

Table A.1. Predicted fluxes for the IRAS 16293−2422 test case.

Transition	Freq. (GHz)	$E_{\rm up}$ ($\rm cm^{-1}$)	A_{ul} ($\rm s^{-1}$)	Line flux ($\rm erg\ s^{-1}\ cm^{-2}$)
$3_{3,0} - 3_{3,1}$	0.824671	233.050	2.12×10^{-12}	2.6×10^{-28}
$5_{0,5} - 4_{2,2}$	3.29676	221.946	4.34×10^{-13}	3.2×10^{-27}
$4_{3,1} - 4_{3,2}$	5.70278	295.677	4.17×10^{-10}	2.1×10^{-25}
$2_{2,0} - 2_{2,1}$	10.2782	109.269	3.63×10^{-9}	1.3×10^{-22}
$3_{2,1} - 4_{1,4}$	20.4600	157.064	9.58×10^{-9}	2.6×10^{-22}
$5_{3,2} - 5_{3,3}$	22.3077	374.409	1.64×10^{-8}	1.7×10^{-23}
$3_{2,1} - 3_{2,2}$	50.2363	157.064	2.08×10^{-7}	1.8×10^{-20}
$4_{3,1} - 5_{2,4}$	61.1859	295.676	2.66×10^{-7}	1.3×10^{-21}
$6_{0,6} - 5_{2,3}$	69.5506	306.312	3.48×10^{-9}	1.2×10^{-22}
$1_{1,0} - 1_{1,1}$	80.5783	32.4939	1.32×10^{-6}	2.7×10^{-18}
$5_{1,5} - 4_{2,2}$	120.778	225.862	1.33×10^{-6}	3.8×10^{-19}
$6_{1,6} - 5_{2,3}$	138.531	308.612	1.43×10^{-6}	9.7×10^{-20}
$4_{2,2} - 4_{2,3}$	143.727	221.832	2.80×10^{-6}	2.6×10^{-19}
$3_{2,1} - 4_{0,4}$	207.111	157.060	1.14×10^{-7}	4.2×10^{-20}
$3_{1,2} - 2_{2,1}$	225.897	116.456	1.31×10^{-5}	7.0×10^{-17}
$2_{1,1} - 2_{1,2}$	241.562	66.1781	1.18×10^{-5}	6.5×10^{-17}
$5_{2,3} - 4_{3,2}$	255.050	303.989	1.78×10^{-5}	1.0×10^{-18}
$2_{2,0} - 3_{1,3}$	266.161	109.262	1.75×10^{-5}	1.0×10^{-17}
$5_{2,3} - 5_{2,4}$	310.533	303.987	1.78×10^{-5}	1.1×10^{-18}
$6_{2,5} - 5_{3,2}$	313.751	384.867	3.75×10^{-5}	1.1×10^{-18}
$3_{3,1} - 4_{2,2}$	335.396	233.016	2.61×10^{-5}	1.2×10^{-18}
$5_{3,2} - 6_{1,5}$	356.836	374.402	3.53×10^{-7}	5.8×10^{-21}
$1_{0,1} - 0_{0,0}$	464.925	15.4975	1.69×10^{-4}	2.5×10^{-15}
$3_{3,0} - 4_{2,3}$	479.947	233.039	7.28×10^{-5}	4.6×10^{-18}
$3_{1,2} - 3_{1,3}$	481.780	116.449	4.74×10^{-5}	2.6×10^{-16}
$2_{0,2} - 1_{1,1}$	490.597	46.1612	5.25×10^{-4}	6.4×10^{-15}
$1_{1,0} - 1_{0,1}$	509.292	32.4844	2.32×10^{-3}	1.8×10^{-15}
$2_{2,0} - 3_{0,3}$	537.793	109.256	9.94×10^{-7}	1.8×10^{-18}
$2_{1,1} - 2_{0,2}$	599.927	66.1706	3.45×10^{-3}	2.9×10^{-15}
$3_{1,2} - 3_{0,3}$	753.411	116.444	5.90×10^{-3}	4.2×10^{-15}
$4_{1,3} - 4_{1,4}$	797.487	182.965	1.31×10^{-4}	3.2×10^{-16}
$4_{1,3} - 3_{2,2}$	827.263	182.964	1.28×10^{-3}	4.2×10^{-15}
$2_{1,2} - 1_{1,1}$	848.962	58.1067	9.27×10^{-4}	1.0×10^{-14}
$1_{1,1} - 0_{0,0}$	893.639	29.7880	8.35×10^{-3}	1.1×10^{-14}
$4_{3,1} - 5_{1,4}$	912.605	295.656	2.74×10^{-6}	2.1×10^{-19}
$2_{0,2} - 1_{0,1}$	919.311	46.1517	1.56×10^{-3}	1.5×10^{-14}
$4_{1,3} - 4_{0,4}$	984.138	182.961	1.07×10^{-2}	5.4×10^{-15}
$3_{0,3} - 2_{1,2}$	995.411	91.3064	7.04×10^{-3}	2.3×10^{-14}
$2_{1,1} - 1_{1,0}$	1009.94	66.1608	1.56×10^{-3}	1.5×10^{-14}
$5_{2,3} - 5_{1,4}$	1161.95	303.968	2.19×10^{-2}	1.6×10^{-15}
$4_{2,2} - 4_{1,3}$	1164.77	221.809	2.00×10^{-2}	3.0×10^{-15}
$5_{1,4} - 5_{1,5}$	1180.32	265.208	2.97×10^{-4}	2.3×10^{-16}
$3_{2,1} - 3_{1,2}$	1217.26	157.036	1.89×10^{-2}	4.4×10^{-15}
$3_{1,3} - 2_{1,2}$	1267.04	100.361	3.91×10^{-3}	2.8×10^{-14}
$2_{1,2} - 1_{0,1}$	1277.68	58.0972	2.19×10^{-2}	3.1×10^{-14}
$2_{2,0} - 2_{1,1}$	1291.64	109.239	1.59×10^{-2}	6.3×10^{-15}
$5_{1,4} - 5_{0,5}$	1297.81	265.206	1.97×10^{-2}	5.4×10^{-15}
$3_{0,3} - 2_{0,2}$	1353.78	91.2989	5.30×10^{-3}	3.6×10^{-14}
$3_{2,2} - 2_{2,1}$	1392.92	155.357	3.25×10^{-3}	7.3×10^{-15}

Table A.1. continued.

Transition	Freq. (GHz)	$E_{\rm up}$ ($\rm cm^{-1}$)	A_{ul} ($\rm s^{-1}$)	Line flux ($\rm erg\ s^{-1}\ cm^{-2}$)
$3_{2,1} - 2_{2,0}$	1432.88	157.032	3.54×10^{-3}	7.2×10^{-15}
$5_{1,4} - 4_{2,3}$	1444.83	265.202	1.02×10^{-2}	8.6×10^{-15}
$4_{0,4} - 3_{1,3}$	1491.93	150.121	3.07×10^{-2}	4.0×10^{-14}
$3_{3,0} - 4_{1,3}$	1500.99	233.016	3.67×10^{-6}	7.9×10^{-19}
$3_{1,2} - 2_{1,1}$	1507.26	116.426	6.58×10^{-3}	3.6×10^{-14}
$2_{2,1} - 2_{1,2}$	1522.93	108.890	2.06×10^{-2}	1.1×10^{-14}
$6_{1,5} - 6_{1,6}$	1615.63	362.469	5.84×10^{-4}	1.5×10^{-16}
$3_{1,3} - 2_{0,2}$	1625.41	100.353	4.49×10^{-2}	5.4×10^{-14}
$3_{2,2} - 3_{1,3}$	1648.80	155.350	3.08×10^{-2}	1.1×10^{-14}
$4_{1,4} - 3_{1,3}$	1678.58	156.343	9.92×10^{-3}	4.1×10^{-14}
$6_{1,5} - 6_{0,6}$	1684.61	362.468	3.47×10^{-2}	4.3×10^{-15}
$4_{0,4} - 3_{0,3}$	1763.56	150.115	1.20×10^{-2}	5.0×10^{-14}
$4_{2,3} - 4_{1,4}$	1818.53	217.000	4.12×10^{-2}	1.0×10^{-14}
$4_{2,3} - 3_{2,2}$	1848.31	216.999	1.06×10^{-2}	1.1×10^{-14}
$4_{3,2} - 3_{3,1}$	1872.61	295.443	6.46×10^{-3}	9.6×10^{-16}
$4_{3,1} - 3_{3,0}$	1877.49	295.634	6.51×10^{-3}	9.7×10^{-16}
$2_{2,1} - 2_{0,2}$	1881.29	108.883	1.21×10^{-4}	7.6×10^{-16}
$3_{2,2} - 3_{0,3}$	1920.43	155.344	3.04×10^{-4}	1.1×10^{-15}
$4_{2,2} - 3_{2,1}$	1941.80	221.791	1.23×10^{-2}	1.1×10^{-14}
$5_{3,3} - 6_{1,6}$	1950.15	373.620	1.11×10^{-5}	9.4×10^{-19}
$5_{3,3} - 6_{1,6}$	1950.15	373.620	1.11×10^{-5}	6.3×10^{-14}
$5_{0,5} - 4_{1,4}$	1965.55	221.900	8.28×10^{-2}	4.2×10^{-14}
$4_{1,3} - 3_{1,2}$	1994.29	182.937	1.66×10^{-2}	4.0×10^{-14}
$4_{2,3} - 4_{0,4}$	2005.18	216.995	5.46×10^{-4}	8.0×10^{-16}
$5_{3,3} - 6_{0,6}$	2019.13	373.618	4.52×10^{-4}	3.9×10^{-17}
$5_{2,4} - 5_{1,5}$	2031.74	293.589	5.43×10^{-2}	7.9×10^{-15}
$6_{1,5} - 5_{2,4}$	2064.69	362.459	4.07×10^{-2}	9.5×10^{-15}
$5_{1,5} - 4_{1,4}$	2083.04	225.816	1.98×10^{-2}	3.4×10^{-14}
$4_{3,2} - 5_{1,5}$	2087.23	295.438	9.50×10^{-6}	1.6×10^{-18}
$5_{3,2} - 5_{2,3}$	2110.99	374.360	8.12×10^{-2}	3.0×10^{-15}
$5_{2,4} - 5_{0,5}$	2149.22	293.587	8.51×10^{-4}	4.5×10^{-16}
$5_{0,5} - 4_{0,4}$	2152.20	221.896	2.23×10^{-2}	4.0×10^{-14}
$4_{3,2} - 5_{0,5}$	2204.71	295.436	3.39×10^{-4}	6.0×10^{-17}
$4_{3,1} - 4_{2,2}$	2213.71	295.626	7.73×10^{-2}	5.3×10^{-15}
$5_{1,5} - 4_{0,4}$	2269.69	225.812	1.36×10^{-1}	5.3×10^{-14}
$3_{3,0} - 3_{2,1}$	2278.02	232.998	5.79×10^{-2}	7.5×10^{-15}
$6_{2,5} - 6_{1,6}$	2286.21	384.822	7.15×10^{-2}	5.4×10^{-15}
$2_{2,1} - 1_{1,0}$	2291.31	108.873	1.26×10^{-1}	3.9×10^{-14}
$5_{2,4} - 4_{2,3}$	2296.25	293.583	2.32×10^{-2}	9.6×10^{-15}
$3_{3,1} - 4_{1,4}$	2297.65	232.970	5.62×10^{-6}	1.8×10^{-18}
$3_{3,1} - 3_{2,2}$	2327.43	232.970	6.09×10^{-2}	7.9×10^{-15}
$5_{3,3} - 4_{3,2}$	2343.74	373.612	1.89×10^{-2}	1.7×10^{-15}
$4_{3,2} - 4_{2,3}$	2351.73	295.432	8.88×10^{-2}	6.0×10^{-15}
$6_{2,5} - 6_{0,6}$	2355.19	384.820	1.23×10^{-3}	2.4×10^{-16}
$5_{3,2} - 4_{3,1}$	2360.34	374.355	1.93×10^{-2}	1.8×10^{-15}
$2_{2,0} - 1_{1,1}$	2382.17	109.214	1.29×10^{-1}	4.4×10^{-14}
$5_{3,3} - 5_{2,4}$	2399.22	373.610	1.07×10^{-1}	4.2×10^{-15}
$6_{0,6} - 5_{1,5}$	2411.83	306.258	1.70×10^{-1}	3.3×10^{-14}
$5_{2,3} - 4_{2,2}$	2463.05	303.938	2.89×10^{-2}	1.0×10^{-14}
$5_{1,4} - 4_{1,3}$	2465.87	265.179	3.27×10^{-2}	2.7×10^{-14}
$6_{1,6} - 5_{1,5}$	2480.81	308.558	3.44×10^{-2}	2.0×10^{-14}
$3_{3,1} - 4_{0,4}$	2484.30	232.966	1.56×10^{-4}	5.1×10^{-17}
$6_{0,6} - 5_{0,5}$	2529.31	306.256	3.67×10^{-2}	2.3×10^{-14}
$6_{1,6} - 5_{0,5}$	2598.29	308.556	2.18×10^{-1}	3.7×10^{-14}
$3_{2,2} - 2_{1,1}$	2674.28	155.327	1.59×10^{-1}	4.8×10^{-14}

Table A.1. continued.

Transition	Freq. (GHz)	$E_{\rm up}$ ($\rm cm^{-1}$)	A_{ul} ($\rm s^{-1}$)	Line flux ($\rm erg\ s^{-1}\ cm^{-2}$)
$6_{2,5} - 5_{2,4}$	2735.28	384.812	4.22×10^{-2}	6.9×10^{-15}
$2_{2,0} - 1_{0,1}$	2810.88	109.204	2.43×10^{-4}	2.2×10^{-15}
$6_{1,5} - 5_{1,4}$	2916.11	362.440	5.53×10^{-2}	1.5×10^{-14}
$3_{2,1} - 2_{1,2}$	2966.08	156.995	1.62×10^{-1}	5.8×10^{-14}
$4_{2,3} - 3_{1,2}$	3015.33	216.972	2.05×10^{-1}	4.6×10^{-14}
$5_{3,3} - 5_{1,4}$	3250.64	373.591	7.43×10^{-4}	9.9×10^{-17}
$5_{2,4} - 4_{1,3}$	3317.29	293.559	2.63×10^{-1}	3.6×10^{-14}
$3_{2,1} - 2_{0,2}$	3324.45	156.988	8.77×10^{-4}	4.6×10^{-15}
$4_{3,2} - 4_{1,3}$	3372.77	295.409	4.06×10^{-4}	1.0×10^{-16}
$3_{3,1} - 3_{1,2}$	3494.45	232.943	1.57×10^{-4}	6.6×10^{-17}
$6_{2,5} - 5_{1,4}$	3586.70	384.793	3.37×10^{-1}	2.4×10^{-14}
$4_{2,2} - 3_{1,3}$	3640.83	221.751	1.96×10^{-1}	5.9×10^{-14}
$3_{3,1} - 2_{2,0}$	3710.07	232.938	6.26×10^{-1}	3.6×10^{-14}
$3_{3,0} - 2_{2,1}$	3721.17	232.965	6.30×10^{-1}	3.5×10^{-14}
$4_{2,2} - 3_{0,3}$	3912.47	221.746	1.99×10^{-3}	4.4×10^{-15}
$3_{3,0} - 3_{1,3}$	3977.05	232.958	1.37×10^{-4}	5.8×10^{-17}
$4_{3,2} - 3_{2,1}$	4149.80	295.391	6.85×10^{-1}	3.4×10^{-14}
$4_{3,1} - 4_{1,4}$	4175.96	295.581	3.25×10^{-4}	8.7×10^{-17}
$4_{3,1} - 3_{2,2}$	4205.74	295.580	7.02×10^{-1}	3.3×10^{-14}
$3_{3,0} - 3_{0,3}$	4248.69	232.953	2.23×10^{-3}	8.7×10^{-16}
$4_{3,1} - 4_{0,4}$	4362.61	295.576	8.17×10^{-3}	2.0×10^{-15}
$5_{2,3} - 4_{1,4}$	4425.31	303.892	2.21×10^{-1}	4.9×10^{-14}
$5_{3,2} - 5_{1,5}$	4453.27	374.306	5.25×10^{-4}	8.5×10^{-17}
$5_{3,3} - 4_{2,2}$	4551.74	373.561	7.54×10^{-1}	3.0×10^{-14}
$5_{3,2} - 5_{0,5}$	4570.75	374.304	1.73×10^{-2}	2.5×10^{-15}
$5_{2,3} - 4_{0,4}$	4611.96	303.888	3.35×10^{-3}	2.6×10^{-15}
$5_{3,2} - 4_{2,3}$	4717.77	374.300	7.96×10^{-1}	2.9×10^{-14}
$3_{3,0} - 2_{1,1}$	5002.54	232.935	4.68×10^{-4}	1.8×10^{-16}
$3_{3,1} - 2_{1,2}$	5243.27	232.902	4.16×10^{-4}	1.5×10^{-16}
$4_{3,1} - 3_{1,2}$	5372.76	295.553	1.32×10^{-3}	3.3×10^{-16}
$3_{3,1} - 2_{0,2}$	5601.64	232.894	3.24×10^{-3}	7.3×10^{-16}
$5_{3,2} - 4_{1,3}$	5738.82	374.277	2.85×10^{-3}	4.7×10^{-16}
$4_{3,2} - 3_{1,3}$	5848.84	295.351	1.02×10^{-3}	1.8×10^{-16}
$4_{3,2} - 3_{0,3}$	6120.47	295.346	1.56×10^{-2}	1.5×10^{-15}
$5_{3,3} - 4_{1,4}$	6514.00	373.515	1.83×10^{-3}	1.8×10^{-16}
$5_{3,3} - 4_{0,4}$	6700.65	373.511	4.38×10^{-2}	2.7×10^{-15}

Appendix B: The low luminosity case: L1448 mm

We present here the results for the case of the low-luminosity source L1448 mm. The density and temperature profiles where derived by Jørgensen et al. (2002).

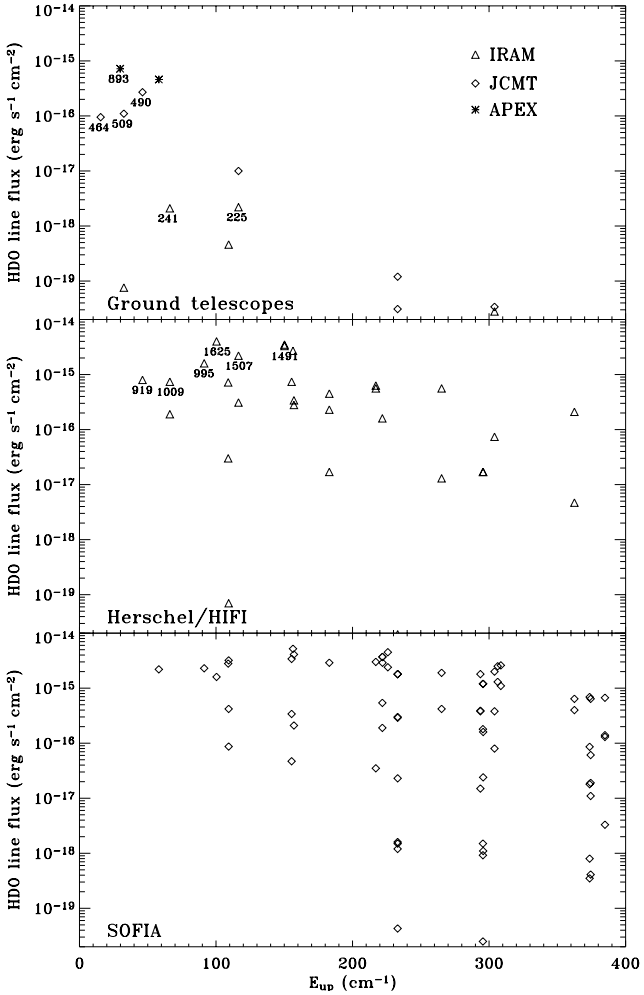

Fig. B.1. HDO line fluxes predicted for the case of the low-luminosity source L1448 mm, for an assumed HDO abundance of 10^{-10} and 10^{-7} in the cold and warm parts of the envelope respectively. The upper panel presents the transitions observable from the ground, the middle panel the transitions observable with HSO/HIFI and the lower panel the transitions observable with SOFIA. The frequencies of the transitions that are going to be studied in more detail are indicated in GHz.

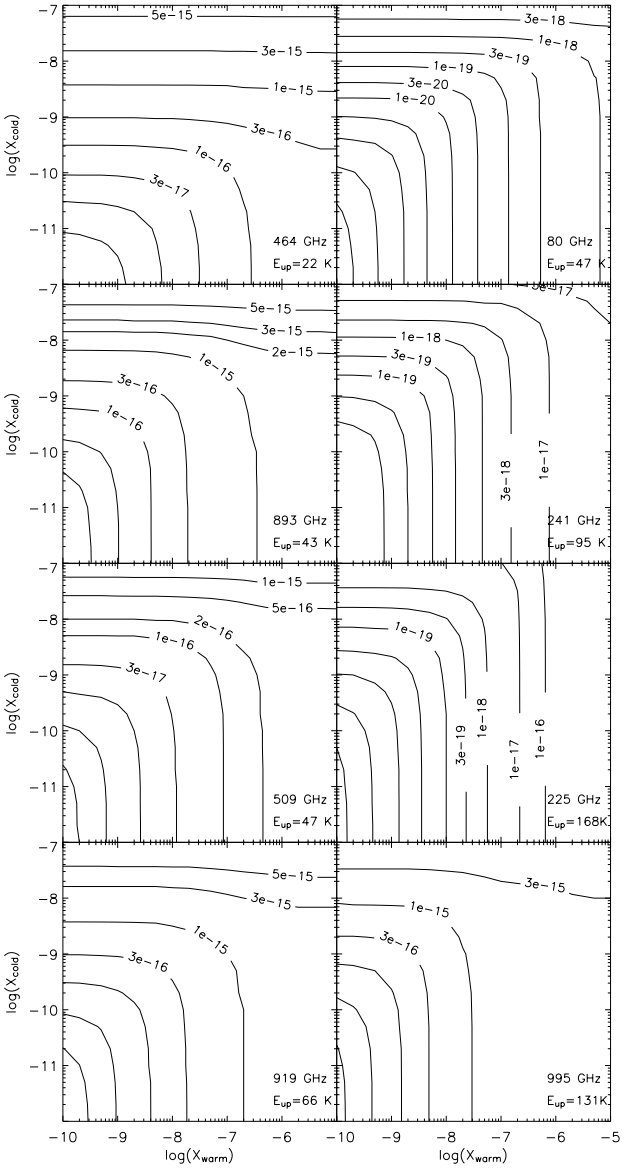

Fig. B.2. Line intensity as a function of the HDO abundance in the outer and inner regions of the envelope, $x_{\rm cold}$ and $x_{\rm warm}$ respectively, for the eight HDO transitions at 464, 893, 509, 80, 241, 225, 919 and 995 GHz respectively towards the low-luminosity source L1448 mm. Line fluxes are in erg s^{-1} cm^{-2}. In these calculations the mantle evaporation temperature is 100 K.

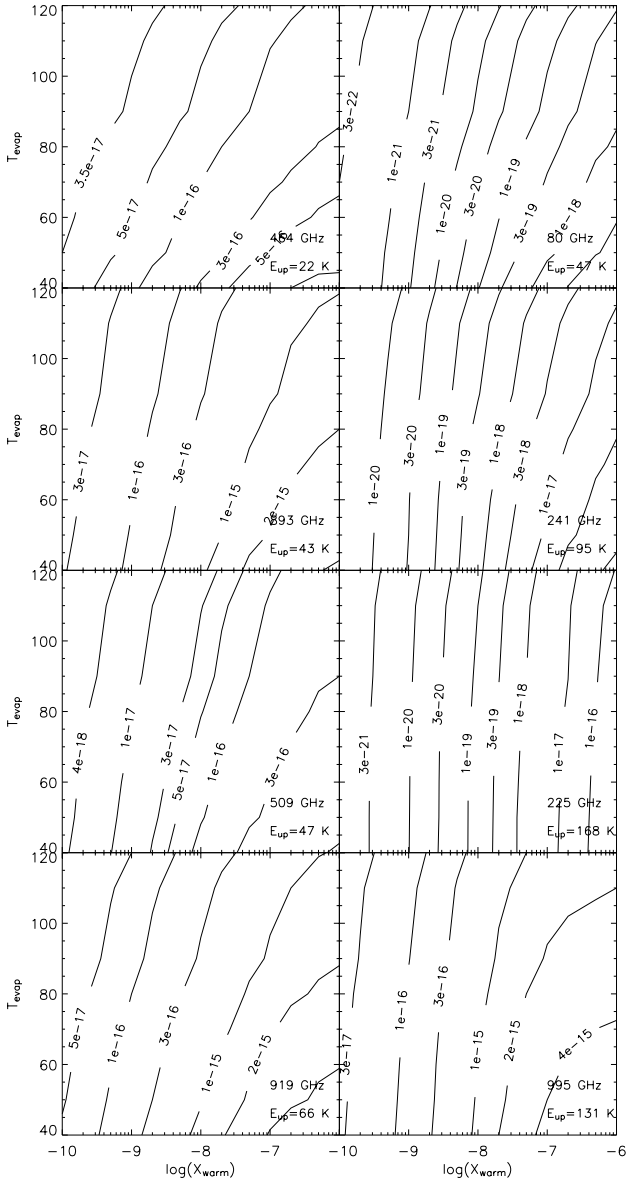

Fig. B.3. Line intensity as a function of the inner HDO abundance and the evaporation temperature, for the eight HDO transitions at 464, 893, 509, 80, 241, 225, 919 and 995 GHz respectively towards the low-luminosity source L1448 mm. Line fluxes are in erg s^{-1} cm^{-2}. In these calculations the outer HDO abundance is 10^{-10}.